Understanding ultrasound neuromodulation using a computationally efficient and interpretable model of intramembrane cavitation

Théo Lemaire[1], Esra Neufeld[2], Niels Kuster[2,3], and Silvestro Micera[1,4]

[1] Translational Neural Engineering Laboratory, Center for Neuroprosthetics and Institute of Bioengineering, School of Engineering, École Polytechnique Fédérale de Lausanne (EPFL), Lausanne, Switzerland

[2] Foundation for Research on Information Technologies in Society (IT'IS), Zurich, Switzerland

[3] Department of Information Technology and Electrical Engineering, Swiss Federal Institute of Technology (ETH), Zurich, Zurich, Switzerland

[4] The Biorobotics Institute, Scuola Superiore Sant'Anna (SSSA), Pisa, Italy

E-mail: silvestro.micera@epfl.ch

Abstract

Objective. Low intensity focused ultrasound stimulation (LIFUS) emerges as an attracting technology for non-invasive modulation of neural circuits, yet the underlying action mechanisms remain unclear. The recently proposed neuronal intramembrane cavitation excitation (NICE) model suggests that LIFUS excites neurons by inducing high-frequency cavitation of resonant plasma membrane structures, thereby generating fast capacitance oscillations that drive depolarizing membrane currents in neighboring ion channels, ultimately triggering action potentials. However, to this effect, the NICE model simulates a complex and computationally expensive electromechanical system with sub-microsecond-scale intra-cycle dynamics. Here, we introduce a novel NICE model variant to achieve fast and accurate simulations and confer interpretability in terms of effective electrical response. ***Approach.*** The NICE system is recast in terms of smoothly evolving differential variables affected by cycle-averaged internal variables that are a function of membrane charge density, stimulus frequency and amplitude. Problem-separation allows to pre-compute lookup tables for these functions, which can be interpolated at runtime to compute electrophysiologically effective, coarse-grained predictions of neural responses. ***Main Results.*** This multi-Scale Optimized Neuronal Intramembrane Cavitation (SONIC) model accelerates computation by more than three orders of magnitude, and accurately captures the millisecond-scale electrical responses of various neuron types while offering an increased interpretability to the effects of ultrasonic stimuli in terms of effective membrane dynamics. Using this model, we characterized the impact of each parameter in the multi-dimensional LIFUS space on the spiking behavior of several neuron types, identified behavioral regimes, and explained observed patterns of spike amplitude and firing rate variation in light of the modified effective electrical system. Furthermore, we used a quasi-steady-state approximation to accurately predict LIFUS-parameter-

dependent and cell-type-specific excitation thresholds, explaining neural activation threshold reduction by low-threshold calcium channels. *Significance.* By providing an electrophysiologically interpretable description, the SONIC model sheds light on cell-type-specific LIFUS neuromodulation according to the intramembrane cavitation hypothesis.

Keywords: Coarse-graining, Computational modeling, Intramembrane cavitation, Neural dynamics, Neuromodulation, Temporal multiscaling, Ultrasound stimulation

---

1. Introduction

Ultrasound (US)-based therapeutic applications, such as diagnostic imaging and thermal ablation therapies, are now widely accepted in the clinical field [1,2]. Low-intensity focused ultrasound stimulation (LIFUS), employing the same technology but with different sonication parameters (carrier frequency, peak pressure amplitude, duration, pulse repetition frequency, and duty cycle), has recently emerged as a very compelling modality for neuromodulation therapies. Owing to their mechanical nature, ultrasonic waves can be accurately directed through biological tissue, offering the ability to concentrate the acoustic energy to a deep focal spot [2,3]. Moreover, numerous experiments on both animal models and humans have demonstrated that transcranial LIFUS is able to either excite, inhibit, or modulate the electrical activity of neurons in the central nervous system (CNS) [4–10]. Furthermore, exhaustive explorations of different sonication parameters on the motor cortex of mice have shown that elicited motor responses are strongly dependent on the amplitude and frequency of the incoming acoustic stimulus [6]. LIFUS could therefore trigger a local and controllable neuromodulatory effect on various neural targets, using a distant and possibly noninvasive sonication device. However, in order for LIFUS to become a reliable neuromodulation technology, we must elucidate the fundamental mechanism(s) by which ultrasonic waves interact with neural tissue at the cellular scale, how these mechanisms may vary across neural structures and how optimal sonication parameters change with it.

Several theories have emerged to try to decipher this interaction. Among them, the neuronal intramembrane cavitation excitation (NICE) model [11] hypothesizes that incoming US waves induce the cavitation of specific nanometer-scale phospholipidic structures within plasma membranes. This model provides quantitative predictions of cell-type-specific neural responses upon ultrasonic exposure that result in excitation or inhibition of cortical networks depending on LIFUS parameters [12]. These predictions agree with the results of numerous in vitro experiments and in vivo studies sonicating the CNS of various animal models [5,6,13–16]. Yet, the model is purely theoretical and built around the intramembrane cavitation hypothesis, whose direct mechanical and electrical manifestations have yet to be observed experimentally. Moreover, the intrinsic electromechanical coupling of the model entails important computational limitations. From an algorithmic standpoint, the explicit modeling of mechanical membrane oscillations with microsecond-scale periodicity results in a very stiff differential system that severely hinders numerical integration.

From an analysis standpoint, the high-amplitude modulation of local transmembrane potential by capacitive oscillations produces a very singular electrical response that can be difficult to interpret under the classical frame of neural dynamics. This computational cost and intrinsic complexity have so far prevented systematic, large-scale explorations of the LIFUS parameter space with the NICE electromechanical model, and its efficient integration in realistic applications involving parallelized resolutions, such as multi-compartmental morphological models and neuron population models.

With these considerations in mind, we sought to develop a coarse-grained variant of the NICE electromechanical model that would allow the interpretation of the millisecond-scale dynamics of neural responses upon ultrasonic exposure in terms of effective membrane dynamics, while significantly decreasing computation times to an acceptable order to magnitude. We then exploited the reduced computational cost and higher abstraction level provided by this multi-Scale Optimized Neuronal Intramembrane Cavitation (SONIC) model to perform an exhaustive characterization of the responses of different neuron types to various combinations of LIFUS parameters.

2. Methods

2.1 The NICE electromechanical model

The NICE electromechanical model [11,12,17] is a mathematical model consisting of a system of first and second-order differential equations describing the dynamic mechanical and electrical behavior of resonant membrane structures that cavitate upon sonication (so-called "bilayer sonophores") and are held together by surrounding transmembrane proteins (figure 1(a)).
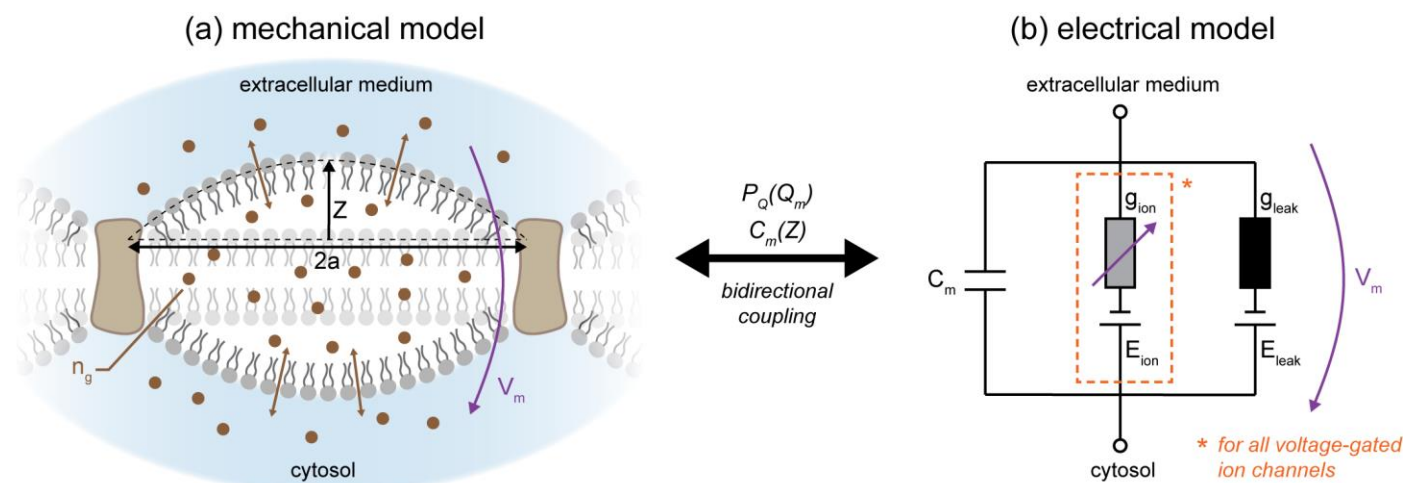

Figure 1. Description of the NICE electromechanical model. (a) Schematic representation of a bilayer sonophore structure (phospholipidic layers, inner cavity and surrounding transmembrane proteins) with the associated differential variables Z (apex deflection) and ng (internal gas molar content). The local transmembrane potential Vm is also indicated. (b) Electrical circuit representation of the local membrane dynamics, with the same transmembrane potential, a deflection-dependent capacitance Cm, and cell-type-specific Hodgkin-Huxley ionic conductances and reversal potentials.

2.1.1 NICE mechanical model.

The mechanical part of the NICE electromechanical model predicts that incoming US waves generate a dynamic pressure imbalance that drives alternating expansions and compressions of sonophore structures, to oscillate at the US frequency. This cyclic behavior is captured by a second-order partial differential equation (akin to the Rayleigh-Plesset equation of bubble cavitation [18]) describing the antiphase apex deflection Z of the sonophore inner and outer leaflets, and a first-order equation describing the variation of internal gas content n_g:

$$(1)$$

$$\frac{d^2Z}{dt^2} = -\frac{3}{2R(Z)}\left(\frac{dZ}{dt}\right)^2 + \frac{1}{\rho_l R(Z)}\left[P_A + P_S(Z) + P_{VS}\left(\left|\frac{dZ}{dt}\right|\right) + P_0 + P_{VL}\left(\left|\frac{dZ}{dt}\right|\right) + P_M(Z) + P_G(Z, n_g) + P_Q(Z, Q_m)\right]$$

$$\frac{dn_g}{dt} = \frac{2S(Z)D_{gl}}{\xi}\left(C_g - \frac{P_G(Z)}{k_H}\right)$$

where $R(Z)$ and $S(Z)$ represent the curvature radius and surface area of a sonophore leaflet and Q_m the local membrane charge density around the sonophore (for a definition of all other parameters see table 1). Ultimately, the normal acceleration of a leaflet apex depends on the resultant of the applied acoustic pressure P_A, the constant hydrostatic pressure P_0 around the membrane, and several intrinsic pressure forces, defined as in [11,17]:

- the elastic membrane tension pressure developed in the two leaflets: $P_S(Z) = -\frac{k_S}{R(Z)}\frac{(S(Z)-S_0)}{S_0}$

- the viscous pressure developing in the leaflets: $P_{VS}\left(\left|\frac{dZ}{dt}\right|\right) = -12\frac{\mu_S \delta_0}{R^2(Z)}\left|\frac{dZ}{dt}\right|$

- the viscous pressure in the extra-membrane medium: $P_{VL}\left(\left|\frac{dZ}{dt}\right|\right) = -4\frac{\mu_l}{R(Z)}\left|\frac{dZ}{dt}\right|$

- the intermolecular pressure between leaflets: $P_M(Z) = \frac{1}{S(Z)}\int_0^{2\pi}\int_0^a A_r\left[\left(\frac{\Delta^*}{2z(r)+\Delta(Q_m)}\right)^x - \left(\frac{\Delta^*}{2z(r)+\Delta(Q_m)}\right)^y\right]drd\theta$

- the internal gas pressure in the cavity: $P_G(Z, n_g) = \frac{n_g R_g T}{V(Z)}$

- the electric pressure exerted on the sonophore by charges on either side of its membrane: $P_Q(Z, Q_m) = \frac{S_0}{S}\frac{Q_m^2}{2\epsilon_0 \epsilon_r}$

Here, S_0 represents the leaflet surface area at rest, $V(Z)$ the sonophore volume, r the in-plane distance from the sonophore center, $z(r)$ the local deflection at this distance, and $\Delta(Q_m)$ the charge dependent gap between the two leaflets of the sonophore when the neuron is at rest (computed by canceling out PM and PQ at Z = 0). All other parameters are defined in table 1.

Table 1. Parameters of the NICE mechanical model.

Parameter	Symbol	Unit	Value	Source(s)
Temperature	T	K	309.15	[19]
Universal gas constant	R_g	Pa·m³·mol⁻¹·K⁻¹	8.314	[20]

Thickness of the leaflet	δ_0	nm	2.0	[17,21]
Gap between the two leaflets on an uncharged membrane	Δ^*	nm	1.4	
Intermolecular pressure coefficient	A_r	Pa	10^5	[17]
Exponent in the intermolecular repulsion term	x	-	5.0	
Exponent in the intermolecular attraction term	y	-	3.3	
Density of the extramembrane medium	ρ_l	kg·m^{-3}	1075	[22]
Dynamic viscosity of the extramembrane medium	μ_l	Pa·s	$7 \cdot 10^{-4}$	[11]
Dynamic viscosity of the leaflet	μ_s	Pa·s	0.035	
Area compression modulus of the bilayer membrane	k_S	N·m^{-1}	0.24	[17,23,24]
Gas concentration in the extra-membrane medium	C_g	mol·m^{-3}	0.62	[11,25,26]
Henry's constant	k_H	Pa·m^3·mol	$1.613 \cdot 10^5$	
Hydrostatic pressure in the extra-membrane medium	P_0	Pa	10^5	[20]
Diffusion coefficient of air in the extra-membrane medium	D_{gl}	m^2·s^{-1}	$3.68 \cdot 10^{-9}$	[27]
Effective thickness of boundary layer between extramembrane medium and intramembrane space for gas transport	ξ	nm	0.5	[11]
Vacuum permittivity	ε_0	F·m^{-1}	$8.854 \cdot 10^{-12}$	[28]
Relative permittivity of the intramembrane cavity	ε_r	-	1	[11]
Resting membrane capacitance	C_{m0}	µF·cm^{-2}	1.0	[19]

2.1.2 NICE electrical model.

The electrical part of the NICE electromechanical model predicts that the alternating expansions and compressions of a cavitating sonophore induce local, periodic oscillations in the plasma membrane capacitance (given by $C_m(Z) = \frac{C_{m0}\Delta}{a^2}\left[Z + \frac{a^2 - Z^2 - Z\Delta}{2Z}\ln\left(\frac{2Z+\Delta}{\Delta}\right)\right]$ as in [11]), which in turn cause large-amplitude oscillations of the transmembrane potential V_m near the resonating structure. The detailed effects of such voltage variations on neuronal excitation are cell-type-specific and captured by a modified Hodgkin-Huxley differential system (figure 1(b)), where the evolution of the local membrane potential V_m depends not only on the contribution of several ionic currents with specific conductances g_{ion} and reversal potentials E_{ion}, but also on a so-called capacitive displacement current ($I_C = V_m \frac{dC_m}{dt}$) originating from the capacitance oscillations:

$$(2)$$

$$\frac{dV_m}{dt} = -\frac{1}{C_m}\left[V_m \frac{dC_m}{dt} + g_{leak}(V_m - E_{leak}) + \sum_{ion} g_{ion}(V_m - E_{ion})\right]$$

$$\frac{dx}{dt} = \begin{cases} \alpha_x(V_m)(1-x) - \beta_x(V_m)\,x \\ \dfrac{x_\infty(V_m) - x}{\tau_x(V_m)} \end{cases}$$

In this system, ionic conductances are regulated by the product of one or multiple gating variables x, whose evolution is regulated by specific voltage-dependent activation and inactivation rate constants (α_x and β_x, respectively), or by a steady state open probability x_∞ and a time constant τ_x (also both voltage-dependent). Sodium (m and h) and delayed

rectifier potassium (n) currents gating variables have been defined with the former paradigm [19], while that of slow non-inactivating (p) and calcium (s and u) currents are defined with the latter one [12,19].

It should be noted that the electric pressure term P_Q depends directly on the membrane charge density, and therefore varies over the course of neural activation. As a result, the mechanical and electrical differential systems are bi-directionally coupled.

2.2 A multi-Scale Optimized Neuronal Intramembrane Cavitation (SONIC) model

The NICE mechanical model (described in [11]) and the Hodgkin-Huxley models of cortical regular spiking (RS), fast spiking, low-threshold spiking (LTS), thalamic reticular, and thalamo-cortical neurons (described in [12]) have been implemented in Python 3.6 and coupled together, using identical equations and parameters as in the references. Numerical simulations of a RS neuron with typical sonophore in-plane radius (32 nm) and LIFUS parameters (500 kHz carrier frequency, 100 kPa pressure amplitude), using the LSODA solver from the scipy.integrate Python library (http://www.scipy.org), revealed the extreme stiffness of the differential system. In consequence, the algorithm required to use many time steps per acoustic period (1000 in our implementation) to ensure stable integration of intra-cycle system oscillations, and resulted in tremendous computation times (>> 1 day for a 150 ms CW stimulus). Therefore, multiple optimization steps were carried out to reduce the computational cost of the algorithm.

2.2.1 Lennard-Jones approximation of intermolecular pressure.

Profiled simulations of the mechanical model in isolation revealed that the spatial integration of intermolecular pressure P_M was by far the longest internal computation at each iteration. However, despite its complexity, this integrated pressure term depends solely on leaflet deflection and the nature of its profile is similar to that of its local counterpart. Therefore, a pre-computing step was defined wherein a Lennard-Jones expression of the form $\widetilde{P_M}(Z) = \widetilde{A_r} \left[\left(\frac{\widetilde{\Delta^*}}{2Z + \Delta(Q_m)} \right)^{\tilde{x}} - \left(\frac{\widetilde{\Delta^*}}{2Z + \Delta(Q_m)} \right)^{\tilde{y}} \right]$ is fitted to the integrated profile and then used as a new predictor of intermolecular pressure during the iterative numerical resolution (figure 2(a)). This simplification allowed to reduce computation times by more than one order of magnitude, without significantly affecting the resulting deflection profiles (RMSE = 0.8 % of cavitation extent over one acoustic period for typical simulation conditions mentioned above).
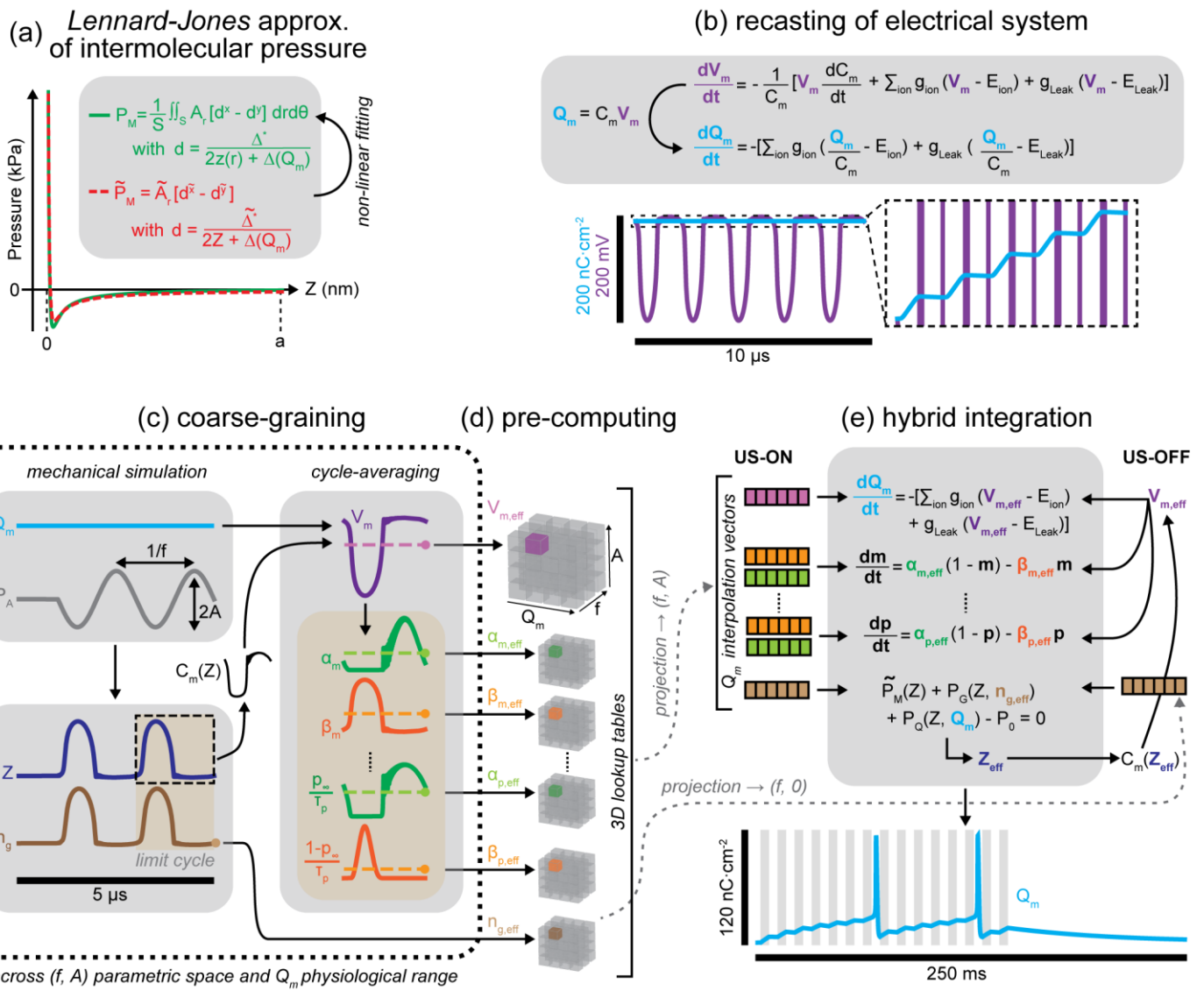
Figure 2. Description of the model simplification and optimization steps. (a) Comparison of spatially integrated (green) and fitted approximation (dashed red) of intermolecular pressure profiles for a realistic range of deflections. (b) Explicit representation of the electrical system recasting, along with a comparison of the short-term evolution of the membrane potential (Vm) and charge density (Qm) upon sonication (500 kHz, 100 kPa), showing remarkably different stiffness. (c-d) Schematic representation of the coarse-graining and pre-computing pipeline. Mechanical simulations are run until periodic stabilization of Z and ng, at which point the membrane capacitance Cm, transmembrane potential and voltage-gated rate constants are computed over the last acoustic cycle. The average value of Vm and rate constants are then stored into lookup tables, along with the final value of ng. The process is repeated for various combinations of US frequencies (f), acoustic pressure amplitudes (A) and membrane charge density. (e) Schematic representation of the hybrid integration of the electrical system. Lookup tables are interpolated at a specific frequency and amplitude to yield interpolation vectors of effective variables in the Qm space, which are then used to integrate numerically the charge-casted electrical system during US-ON periods. The effective gas content is also updated at all times (requiring to project an extra ng interpolation vector at zero amplitude) to compute a charge and gas content dependent effective membrane capacitance which is then used to integrate the system during US-OFF periods by calculating the membrane potential and voltage-gated rate constants.

2.2.2 Recasting of the electrical system.

Simulations of the detailed NICE electromechanical model predict that while the local membrane potential of a cavitating sonophore undergoes large-amplitude oscillations, the membrane charge density and the ion channel gating variables around that structure evolve much more smoothly over the course of neural activation ([11] and figure 2(b)). Therefore, the electrical system was first recast as function of charge (using the transformation $Q_m = C_m V_m$), thereby removing the capacitive displacement current term and yielding a new scheme composed only of smooth differential variables:

(3)

$$\frac{dQ_m}{dt} = -\left[g_{leak}\left(\frac{Q_m}{C_m} - E_{leak}\right) + \sum_{ion} g_{ion}\left(\frac{Q_m}{C_m} - E_{ion}\right) \right]$$

$$\frac{dx}{dt} = \begin{cases} \alpha_x\left(\dfrac{Q_m}{C_m}\right)(1-x) - \beta_x\left(\dfrac{Q_m}{C_m}\right)x \\ \dfrac{x_\infty\left(\dfrac{Q_m}{C_m}\right) - x}{\tau_x\left(\dfrac{Q_m}{C_m}\right)} \end{cases}$$

As Q_m/C_m is still rapidly oscillating, the evolution of electrical differential variables during US-ON periods was then expressed as a function of "effective" internal variables (using this time the rate constants formulation for all gates, with $\alpha_x = x_\infty/\tau_x$ and $\beta_x = 1/\tau_x - \alpha_x$), obtained by averaging their rapid oscillatory part over an acoustic period T. This is only possible because the differential variables evolve smoothly and allows to capture the millisecond-scale system evolution without explicitly resolving intra-cycle oscillations:

(4)

$$\left(\frac{dQ_m}{dt}\right)_{eff} = -\left[g_{leak}\left(\underbrace{\frac{\int_0^T \frac{Q_m}{C_m(Z)}dt}{T}}_{V_{m,eff}} - E_{leak} \right) + \sum_{ion} g_{ion}\left(\underbrace{\frac{\int_0^T \frac{Q_m}{C_m(Z)}dt}{T}}_{V_{m,eff}} - E_{ion} \right) \right]$$

$$\left(\frac{dx}{dt}\right)_{eff} = \underbrace{\frac{\int_0^T \alpha_x\left(\frac{Q_m}{C_m(Z)}\right)dt}{T}}_{\alpha_{x,eff}}(1-x) - \underbrace{\frac{\int_0^T \beta_x\left(\frac{Q_m}{C_m(Z)}\right)dt}{T}}_{\beta_{x,eff}}x$$

We shall refer to $V_{m,eff}$ as the effective membrane potential and to $\alpha_{x,eff}$ and $\beta_{x,eff}$ as effective rate constants. As they depend directly on the sonophore deflection profile and thus indirectly on the LIFUS parameters and the electro-mechanical coupling, effective variables were pre-computed for various combinations of ultrasonic frequencies (f), acoustic peak pressure amplitudes (A) and membrane charge densities – covering the LIFUS parametric space and membrane physiological range – and then stored in 3D lookup tables to be linearly interpolated at runtime (figure 2(c-d)). For each combination, a short simulation of the mechanical system was performed until a limit cycle was reached (detected by thresholding the root mean square error between two consecutive cycles of both Z and n_g), and effective variables were then computed over the last acoustic cycle. The required granularity of lookup tables was determined by visually inspecting the nonlinearity of effective variables along each dimension. We computed lookups for 7 characteristic carrier frequencies over the 20 kHz – 4 MHz range (20, 100 and 500 kHz, 1, 2, 3 and 4 MHz), 50 logarithmically distributed pressure amplitudes between 0 and 600 kPa, and cell-type-specific ranges of physiologically realistic, linearly distributed charge densities (1 nC/cm^2 step).

8

2.2.3 Hybrid integration.

The formulation of an effective coarse-grained electrical system (equation (4)) removed the need to compute the evolution of deflection and gas content during US-ON periods, as the electro-mechanical coupling was effectively decoupled during pre-computation steps. However, as membrane capacitance is directly dependent on these two mechanical variables, especially in the absence of acoustic perturbation, they must be tracked in order to integrate US-OFF periods in an accurate manner. Hence, the effective evolution of internal gas content $n_{g,eff}$ (also pre-computed and interpolated at runtime) was considered and defined as the gas content at the end of an acoustic cycle rather than as a cycle-averaged value since ON-OFF transitions necessarily occur at such instants. Membrane capacitance during US-OFF periods was then computed by solving the transcendental equation $\widetilde{P_M} + P_G + P_Q - P_0 = 0$ for Z as in [17], i.e. by computing the equilibrium deflection for a mechanical system assumed to be in a quasi-steady state where viscoelastic stresses are negligible.

Using these transformations, effective solutions were computed by integrating alternatively equations (3) and (4) during US-OFF and US-ON periods respectively (figure 2(e)). We used the same LSODA solver as for the detailed NICE model, however the absence of rapid oscillations allowed us to use a constant time step far greater than a typical acoustic period (dt = 50 µs). For the sake of simplicity, this new model variant involving electrical system recasting and coarse-graining, pre-computation of effective variables and hybrid numerical integration using lookup interpolation tables will be referred to as SONIC model later on.

2.2.4 Validation against the detailed electromechanical model.

The accuracy of the SONIC model was evaluated by comparing membrane charge density profiles of effective simulations to those of detailed simulations (based on the charge-casted NICE electromechanical model described in equations (1) and (3)) for a variety of LIFUS conditions. Spikes were detected on the charge density profiles by a peak-prominence thresholding approach in order to derive relevant metrics (latency, firing rate and spike amplitude) that were used for further quantitative comparisons. We first tested the ability of the coarse-grained system to capture both sub-threshold passive responses and supra-threshold tonic firing responses of a RS neuron for a wide range of acoustic amplitudes and frequencies under continuous-wave (CW) stimulation. We then evaluated the ability of the combined coarse-grained and charge-casted systems to capture sub and supra-threshold responses of RS and LTS neurons under pulsed-wave (PW) stimulation, for various duty cycles and pulse repetition frequencies, as these neurons are representative of the two main types of sensitivities to pulsed LIFUS protocols according to predictions from the NICE model [12]. The validation results and conclusions about the limits of the SONIC model can be found in the Results section.

2.3 Efficient and interpretable characterization of neural responses

2.3.1 Systematic exploration of the LIFUS parameter space.

A typical LIFUS protocol comprises five distinct stimulation parameters: US frequency (f), acoustic peak pressure amplitude (A), pulse-repetition-frequency (PRF), duty-cycle (DC), and duration, all of which affect substantially the mechanical and electrical response of a neuron. The latter also depends heavily on the cell-type-specific ion channel population and on the acoustic properties of its immediate anatomical environment. Hence, LIFUS optimization is a complex problem that requires the exhaustive characterization of the effects of multiple, possibly co-dependent, parameters over a high-dimensional space – a challenge that goes far beyond what is experimentally feasible. In this context, computational models can constitute a powerful tool to study the effect of a specific set of parameters in an isolated manner, provided they can be used efficiently.

Taking advantage of the drastic reduction in computational burden associated with the SONIC model, systematic explorations of the LIFUS space was performed for different cell types by varying the following stimulation parameters: US frequency, acoustic peak pressure amplitude, pulse-repetition-frequency and duty-cycle. Stimulus duration was fixed to one second in order to analyze all relevant features of neural responses (excitation thresholds, spike rate adaptation, bursting behaviors, etc.). Relevant metrics (i.e., occurrence of spike(s) and firing rate) were derived from the charge profile of each simulation, and two-dimensional behavior maps were generated using duty cycle and pressure amplitude as the two primary dimensions, since neural activation across cell types was found to be mostly sensitive to these parameters.

2.3.2 Quasi-steady state approximation of excitation thresholds.

A widely accepted conjecture in the field of classical neuro-physiology is that spikes are generally triggered when the membrane potential of a neuron crosses a threshold value V_T, as the result of electrical stimulation or physiological activity. In the context of intramembrane cavitation, this conjecture is obviously unreasonable, as US-induced potential oscillations cross the threshold multiple times without necessarily prompting neural activation. However, we can transpose it to the smoothly evolving membrane charge density by postulating that neural excitation would occur whenever Q_m crosses a threshold value Q_T. It can also be reasonably assumed that (i) there exists a minimal acoustic pressure amplitude A_T - analog to a rheobase current - such that only a stimulus of infinite duration at that amplitude results in Q_T being reached, (ii) as we let the stimulus amplitude tend towards A_T from a sub-threshold range, the membrane charge density converges asymptotically towards Q_T, (iii) within this asymptotical regime, the charge density and the conductances of voltage-gated ion channels do not evolve significantly during a pulse repetition interval, and (iv) these variables vary linearly within the LIFUS-ON and LIFUS-OFF periods of this interval. We then obtain the following quasi-steady state conditions:

(5)

$$\left[g_{leak}\left(V_{m,eff}(f, A, Q_T) - E_{Leak}\right) + \sum_{ion} g_{ion}\left(V_{m,eff}(f, A, Q_T) - E_{ion}\right) \right] DC$$

$$+ \left[g_{leak}\left(\frac{Q_T}{C_m} - E_{Leak}\right) + \sum_{ion} g_{ion}\left(\frac{Q_T}{C_m} - E_{ion}\right) \right] (1 - DC) = 0$$

$$\left[\alpha_{x,eff}(f, A, Q_T)\, DC + \alpha_x\left(\frac{Q_T}{C_m}\right)(1 - DC) \right](1 - x) - \left[\beta_{x,eff}(f, A, Q_T)\, DC + \beta_x\left(\frac{Q_T}{C_m}\right)(1 - DC) \right] x = 0$$

Cell-type-specific frequency and duty-cycle-dependent threshold amplitudes curves were computed with equation (5), using $C_m = 1$ µF/cm^2 (the resting membrane capacitance), V_T as neuron-specific spike threshold parameters specifically adjusted against experimental data [19,29,30] and $Q_T = C_m V_T$. To do so, effective variables were interpolated from the generated lookup tables along the amplitude dimension at f and Q_T, thus generating a vector of amplitude-dependent quasi-steady state charge variation (figure 3(a)). Subsequently, interpolated root-finding allows to determine the threshold amplitude (figure 3(b-c)).
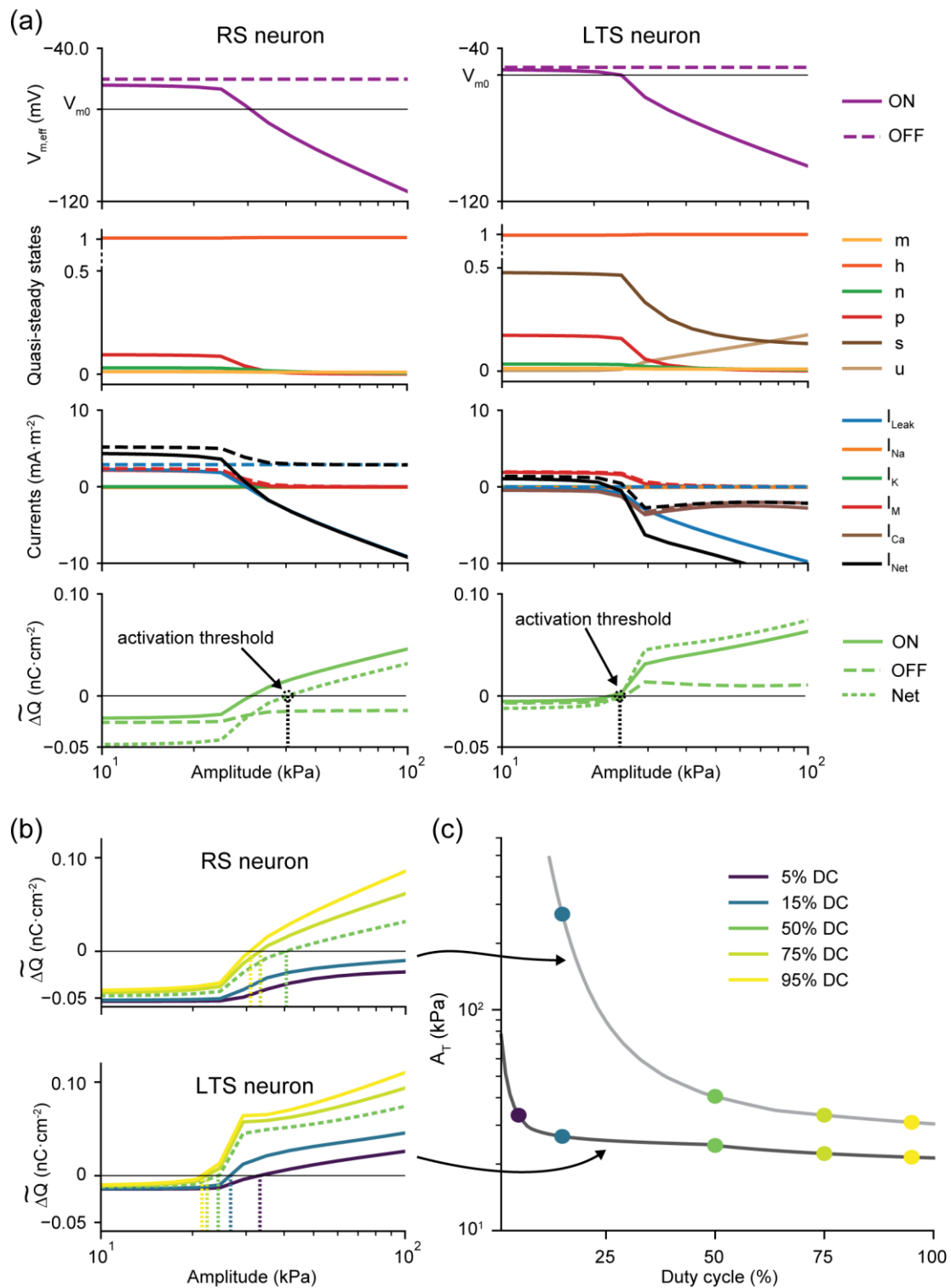
Figure 3. Quasi-steady state approximation of threshold membrane dynamics. (a) Effective membrane potential, quasi-steady gating variables, approximated membrane currents, and charge density variations of regular spiking and low-threshold spiking neurons during US-ON (plain lines) and US-OFF (dashed lines) periods of a pulse repetition interval (100 Hz PRF, 50% duty cycle) as a function of acoustic pressure amplitude, evaluated at their respective threshold charge density. (b) Comparison of approximated net charge variations (plain lines) at QT during a pulse repetition interval (100 Hz PRF) at different characteristic duty cycles, for regular spiking (top) and low-threshold spiking (bottom) neurons, along with the resulting threshold excitation amplitudes (dashed vertical lines). (c) Threshold excitation amplitudes computed from quasi-steady state approximation as a function of duty cycles for both neurons. Scatter dots indicate the characteristic duty cycles evaluated in (b).

3. Results

3.1 LIFUS modulation of effective variables

3.1.1 Effective membrane potential.

In the absence of acoustic perturbation, the mechanical state of the sonophore is solely dependent on gas content and charge density. As the latter increases in magnitude, augmentation of the electrical pressure compresses the sonophore and increases its membrane capacitance. As a result, the profile of the unperturbed effective membrane potential $V_{m,eff}$ = Q_m/C_m is an odd function of Q_m that deviates slightly from linearity (figure 4(a)). For small acoustic perturbations (A < 50 kPa), the amplitude of intra-cycle oscillations is still heavily dependent on the electrical pressure. Hence, the sonophore expansions and the resulting capacitance drops throughout acoustic cycles are considerably reduced as the magnitude of membrane charge density increases. Thus, the cycle-averaged capacitance displays an inverse bell-shaped profile as a function of charge (figure 4(a), inset), and the resulting effective membrane potential, despite conserving its odd symmetry, is amplified at intermediate values of $|Q_m|$ before converging asymptotically towards its unperturbed counterpart as charge magnitude is further increased. Larger acoustic perturbations (A > 50 kPa) induce greater sonophore expansions and capacitance drops within intra-cycle oscillations, during which the influence of the electrical pressure is heavily reduced. This means that the profile of cycle-averaged membrane capacitance is shifted towards lower values and exhibits little dependency on the charge density within the physiological range. Consequently, the $V_{m,eff}$ charge profile is amplified and transitions towards another regime. In summary, the effective membrane potential is an odd function of charge density, amplified as acoustic pressure amplitude increases, and transitioning nonlinearly between two pseudo-linear regimes within the charge physiological range. This amplification generates larger deviations from reversal potentials, and thus stronger ionic currents.
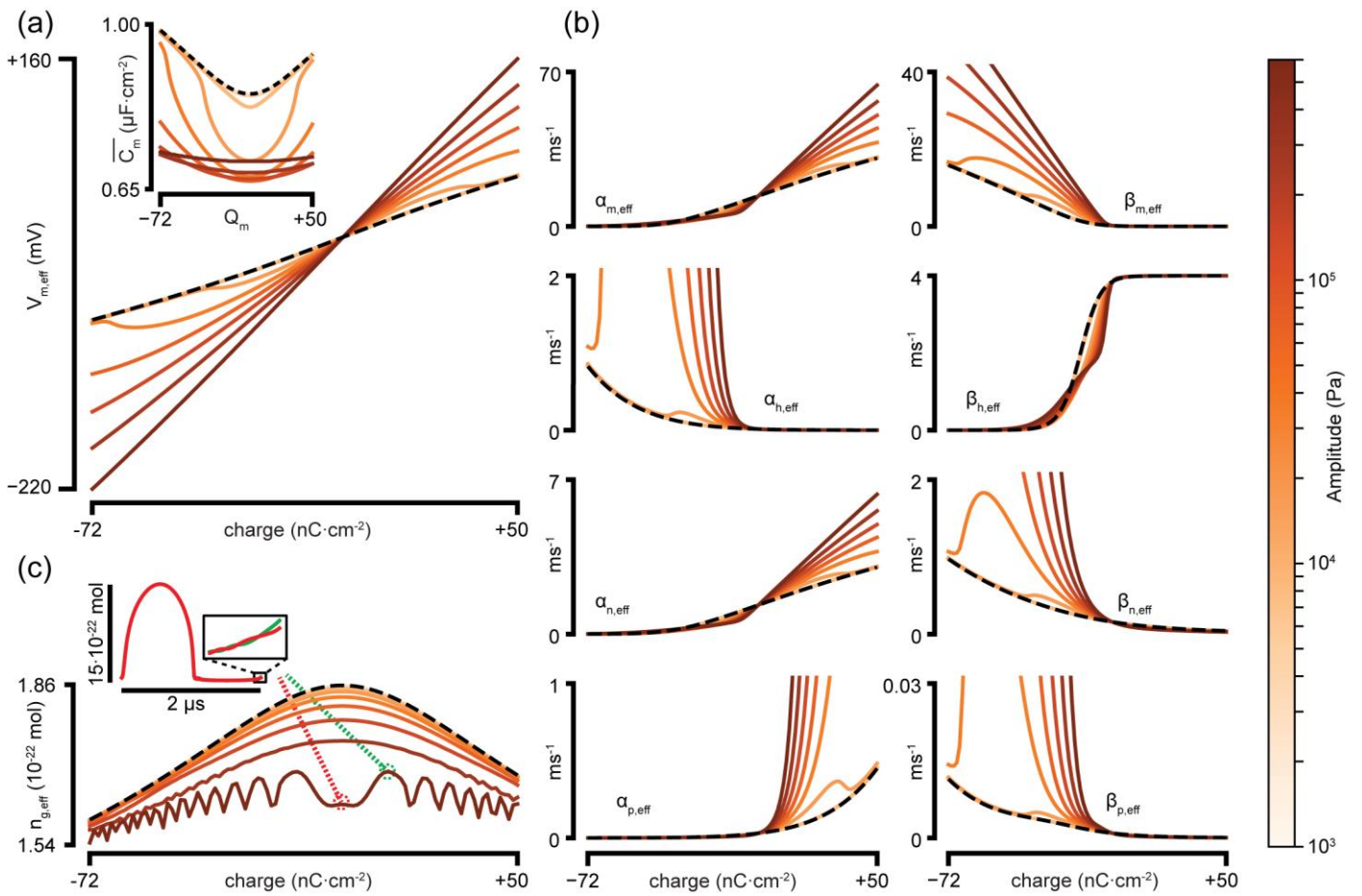
Figure 4. Modulation of charge dependent effective variables as a function of acoustic pressure amplitude. Effective variables of a regular spiking neuron at 500 kHz are displayed as a function of membrane charge density, with a color code corresponding to the acoustic pressure amplitude at which they were derived (color bar depicted on the right side). The original, non-modulated variables (dashed black lines) are also depicted for comparison. (a) Effective membrane potential, with an inset showing the cycle-averaged capacitance profiles at the same amplitudes. (b) Ion channel gating rate constants of the RS neuron. (c) Internal molar gas content, with an inset showing detailed temporal profiles of gas content over the last acoustic cycle for two specific charge values at 600 kPa amplitude.

3.1.2 Effective rate constants.

As voltage-gated rate constants are nonlinear functions of the membrane potential, their effective counterparts cannot be derived directly from $V_{m,eff}$ and must be explicitly computed (figure 4(b)). For small acoustic perturbations, they also deviate from their original counterpart at intermediate charge values and re-converge asymptotic towards it as we reach the borders of the physiological range. For large acoustic perturbations, all profiles are widely amplified around one extremity of the range due to their exponential nature, with the exception of the sigmoidal β_h profile. In particular, $\alpha_{m,eff}$ and $\alpha_{n,eff}$ are amplified for positive charge values which will lead to faster openings of the sodium m-gate and potassium n-gate during action potentials. Hence, LIFUS modulation also amplifies rate constants and increases their nonlinearity, which is likely to trigger faster gating variations.

3.1.3 Effective gas content.

In the absence of acoustic perturbation, the sonophore gas content is inherently dependent on its volume. As the sonophore is compressed upon an increase in $|Q_m|$ because of the higher electrical pressure, the original gas content profile is an even function of the charge density (figure 4(c)). Upon acoustic perturbation, the intra-cycle evolution of n_g

follows the sonophore oscillations, augmenting during expansion phases and decreasing during compressions, with a small, yet non-zero intrinsic inertia. As a result, the gas content at the end of the compression phase (arbitrarily defined as the end of an acoustic cycle) is still slightly lower than its resting value. As this effect is amplified by the magnitude of mechanical oscillations, the charge profile of effective gas content $n_{g,eff}$ decreases as the acoustic pressure amplitude increases. For very strong perturbations (A > 100 kPa), mechanical resonance of the sonophore all throughout compression phases induce high-frequency oscillations in the evolution of gas content until the end of the acoustic cycle (figure 4(c), inset). As the electrical pressure influences the synchronization between n_g and the acoustic wave, the phase of those oscillations at the end of the acoustic cycle ultimately depends on the magnitude of charge density, and introduces subsequent oscillations in the charge profile of $n_{g,eff}$. Thus, despite slightly decreasing with rise in the absolute charge density and acoustic pressure amplitude, the effective gas content experiences very little variations upon LIFUS modulation or changes in the membrane electrical state.

3.2 SONIC model validation

Under typical CW LIFUS conditions (500 kHz carrier frequency, 150 ms stimulus), the SONIC model accurately captures both passive responses of a RS neuron at sub-threshold amplitudes (figure 5(a), blue traces) and non-adaptive high-frequency tonic spike trains elicited at supra-threshold amplitudes (figure 5(a), red traces). In the latter regime, amplitude dependent variations in response latency, firing rate, and spike amplitude within the tonic train are picked up with a remarkable accuracy up to 600 kPa (figure 5(a), metrics chart), a value far exceeding the pressure amplitudes used in recent neuromodulation studies on the central nervous system [31]. However, the model fails to capture the exact threshold amplitude at which the neuron transitions from a passive response to an active spiking behavior: integration with the detailed NICE model does not yield excitation at the threshold amplitude determined by a titration procedure with the SONIC model (figure 5(a), green traces). It can be assumed that this arises from the high nonlinearity of the effective membrane potential at low acoustic pressure amplitudes and negative charge densities (figure 4(a)), yielding inaccurate linear interpolations during the build-up phase.
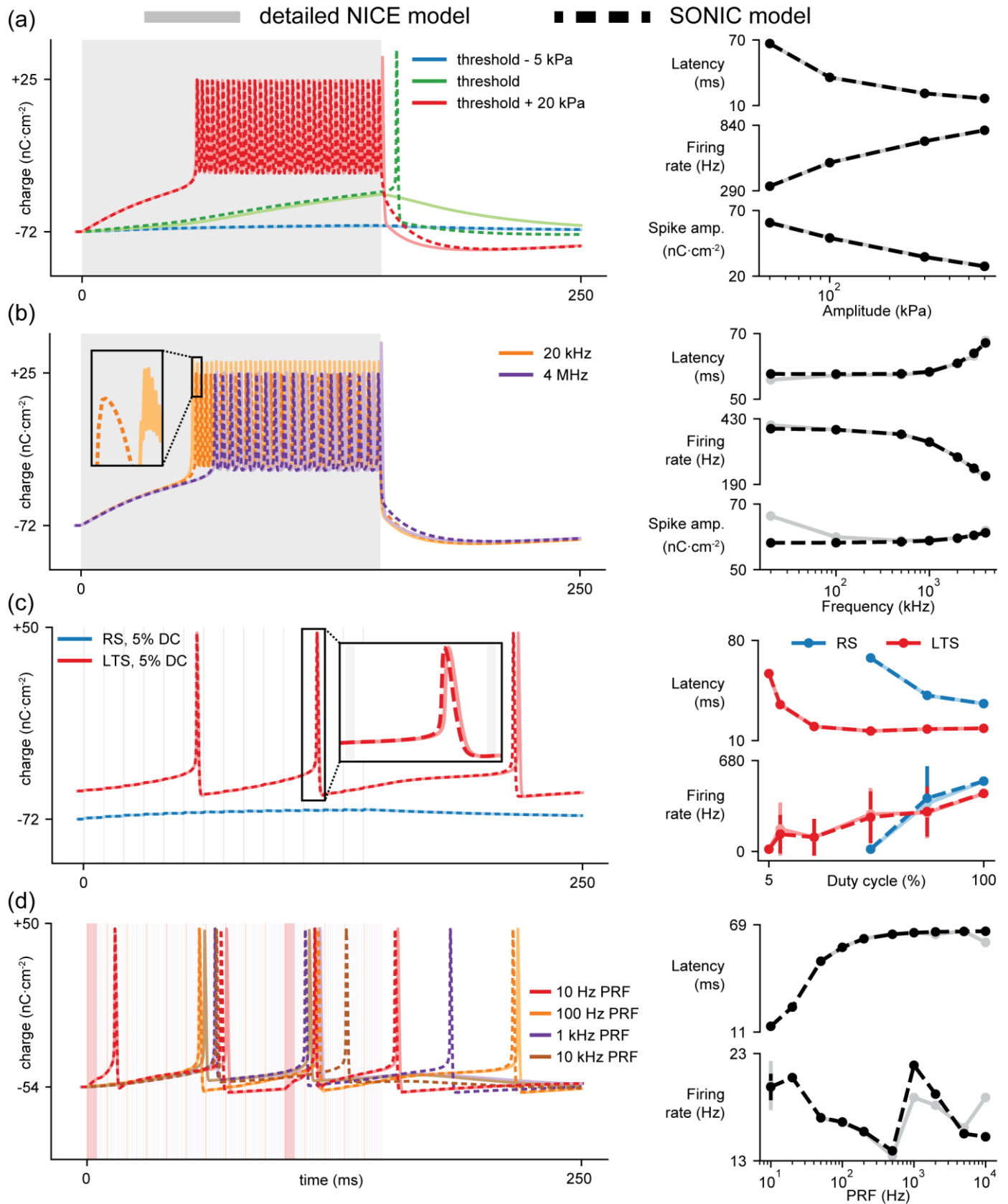
Figure 5. Validation of the SONIC model against the detailed NICE model. Membrane charge density profiles from simulations with the detailed NICE model (light solid curves) and SONIC model (dark dashed curves) of different neurons (32 nm sonophore radius) under various LIFUS conditions are compared, along with derived spiking metrics (latency, firing rate and spike amplitude). (a) Left: comparison of charge density profiles of a RS neuron under CW-sonication (500 kHz carrier frequency) for sub-threshold, threshold and supra-threshold acoustic pressure amplitudes. Right: comparison of derived spiking metrics for varying supra-threshold pressure amplitudes. (b) Left: comparison of charge density profiles of a RS neuron under CW-sonication at supra-threshold amplitude (threshold + 20 kPa) with 20 kHz and 4 MHz carrier frequencies. Right: comparison of derived spiking metrics for varying carrier frequencies from 20 kHz to 4 MHz. (c) Left: comparison of charge density profiles of RS (blue) and LTS (red) neurons under pulsed-wave sonication (500 kHz, 100 kPa, 100 Hz PRF) at 5 % duty cycle. Right: comparison of derived spiking metrics for varying duty cycles

from 5 – 100 %. (d) Left: comparison of charge density profiles of a LTS neuron under pulsed-wave sonication (500 kHz, 100 kPa, 5 % DC) at 10 Hz, 100 Hz, 1 kHz and 10 kHz pulse repetition frequencies. Right: comparison of derived spiking metrics for varying pulse repetition frequencies from 10 Hz to 10 kHz.

The model accuracy for supra-threshold amplitudes is conserved as the carrier frequency increases up to several MHz (figure 5(b), purple traces). However, significant differences in spike amplitude (and to a lesser extent in latency and firing rate) appear as the frequency approaches the lower bound of the ultrasonic domain (figure 5(b), metrics chart). In fact, at such low frequencies, the order-of-magnitude of the intra-cycle oscillations dynamics approaches that of the gating kinetics of sodium and potassium ion channels, thereby inducing large intra-cycle gating variations that modulate the membrane charge density at the US frequency and cause considerable oscillations in the detailed solution (figure 5(b), inset). As can be expected, these oscillations are absent from the effective solution because of the intrinsic cycle-averaging strategy of the SONIC model, but the resulting spiking behavior stays qualitatively correct. This intra-cycle interference (and the resulting divergence) vanishes at frequencies higher than 100 kHz. Thus, the SONIC model can estimate cell-type-specific threshold excitation amplitudes with a precision in the order of kPa, and accurately captures the amplitude and frequency dependencies of neural responses to CW stimuli. Note that these observations translate to other neuron types since they all share the same mode of interaction with CW stimuli (data not shown).

Under typical PW stimulation conditions (500 kHz, 100 kPa, 100 Hz PRF), the SONIC model accurately captures cell-type-specific, duty-cycle dependent changes in latency and firing rate of RS and LTS neurons. In particular at very low duty cycles, both the passive response of a RS neuron and the sparse firing of a LTS neuron are accurately obtained (figure 5(c), blue and red traces). In the latter case, a minor divergence is initiated and amplified during US-OFF periods (figure 5(c), inset), which is likely due to the great sensitivity of the charge-casted system to initial conditions of early depolarization phases as well as intrinsic differences in the computation of membrane capacitance between the NICE and SONIC models. This divergence is also found for the RS neuron that starts firing at 50 % duty cycle and yields small inaccuracies in the reported firing rates (figure 5(c), metrics chart), despite producing very similar spiking behaviors. This similarity is mostly preserved throughout variations in pulse repetition frequency for a LTS neuron at 5 % duty cycle (figure 5(d), traces and metrics chart), with two notable exceptions at 1 kHz and 10 kHz. In the former case, the model inaccuracy is probably due to a particular pulse-spike synchronization that amplifies divergence of the effective solution – in fact, a slight divergence in the charge build-up phase can shift spike occurrence by one or several pulses, thereby offsetting the entire downstream response dynamics. In the latter case, however, divergence likely arises from the increasing number of ON-OFF transitions and the decrease of pulse duration down to the order of magnitude of the integration time step of the SONIC model, limiting the number of iterations per pulse and thereby the accuracy of the effective solution. Thus, the SONIC model accurately captures the duty cycle and PRF dependencies of cell-type-specific neural responses to PW stimuli, relevant to different gating mechanisms.

3.3 Acceleration quantification

We assessed the algorithmic acceleration provided by the presented SONIC model by comparing computation rates (i.e., simulated duration divided by computation time) with detailed NICE simulations on the same computer (24-core, 2.1 GHz clock rate server, 126 GB RAM, Ubuntu 16.04.3 operating system).

For typical CW stimulation parameters (500 kHz carrier frequency), NICE and SONIC model solutions are computed at rates in the order of 10^{-3}-10^{-2} and 10^{1}-10^{2} ms-stim/s-comp, respectively, across the five tested neuron types (figure 6(a)). Interestingly, computation rates of both model variants are 2-3 times lower for supra-threshold stimuli than for sub-threshold stimuli, despite a rather small relative change in acoustic pressure amplitude and resultant intra-cycle oscillations between the two conditions. This illustrates the stiffer differential system resulting from an active electrical response, as the employed LSODA solver uses an adaptive integration scheme that takes an increasing number of internal steps at each iteration as the system stiffness augments. Within the supra-threshold regime, computation rates of the NICE model decrease as pressure amplitude increases, because of the increased stiffness of its intrinsic differential system for larger intra-cycle oscillations, requiring more internal steps to be taken at each iteration (figure 6(b)). Computation rates of the SONIC model also show a weak dependency on the stimulus amplitude despite neglecting intra-cycle oscillations, further illustrating the non-negligible influence of electrical variables on the system's stiffness. Expectedly, computation rates of the NICE model decrease as the stimulus carrier frequency increases owing to the algorithm's frequency-dependent integration time step, while those of the SONIC model do not exhibit any dependency on that parameter (figure 6(c)). For PW stimuli, NICE computation rates decrease as the stimulus duty cycle increases, for both actively and passively responding neurons (figure 6(d)). Interestingly, SONIC computation rates only show little sensitivity to the duty cycle value, despite the intrinsic differences in computation of internal variables between ON and OFF periods. Moreover, computation rates of both algorithms for the activated LTS neuron at 5% duty cycle are on average half that of the passively responding RS neuron, thereby confirming the influence of electrical variables on the system's stiffness. In conclusion, the presented SONIC model accelerates computation times by more than three orders of magnitude – sometimes more than four – across all tested conditions, and its algorithmic efficiency shows less sensitivity to changes in stimulation parameters.
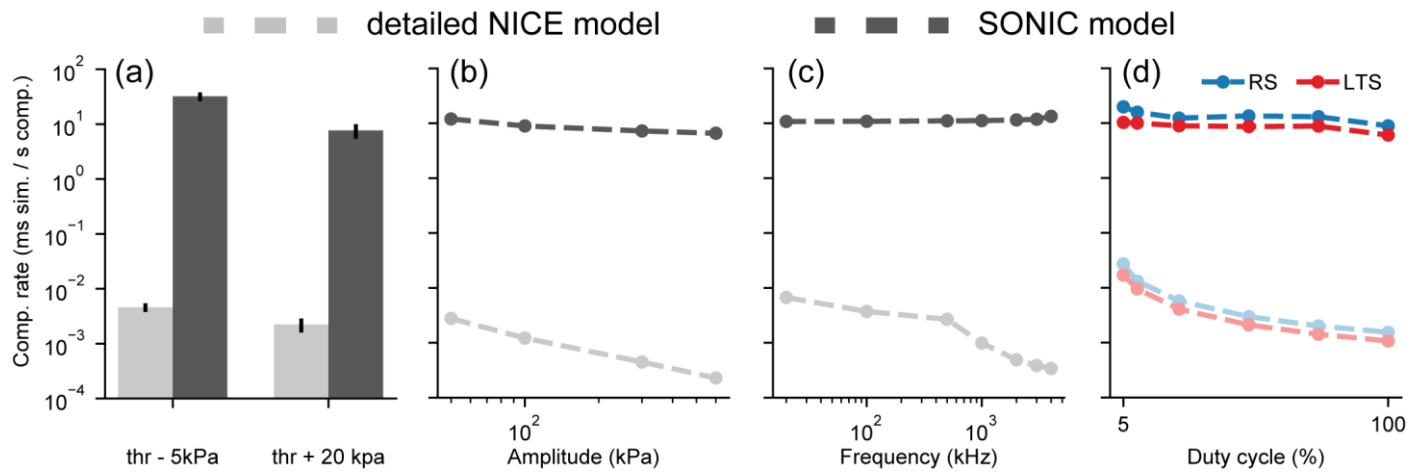
Figure 6. Quantification of the SONIC model acceleration. Comparison of computation rates of the detailed NICE (light gray) and SONIC (dark gray) models for various LIFUS conditions. (a) Rates comparison for continuous-wave simulations of the five implemented neuron types at sub-threshold (threshold - 5 kPa) and supra-threshold (threshold + 20 kPa) acoustic amplitudes. (b) Rates comparison for continuous-wave simulations of the RS neuron at various supra-threshold acoustic amplitudes. (c) Rates comparison for continuous-wave simulations of the RS neuron at various ultrasonic frequencies with a supra-threshold amplitude (threshold + 20 kPa). (d) Rates comparison for simulations of the RS (blue) and LTS (red) neurons (500 kHz, 100 kPa, 100 Hz PRF) at various duty cycles.

3.4 Cell-type-specific behavior maps

The NICE electromechanical model predicts that cell-type-specific sensitivities to LIFUS can be classified into two main categories, depending on the presence or absence of a voltage-gated depolarization current active at sub-threshold charge levels [12]. Therefore, our analysis focused on the RS and LTS neurons that provide a typical use case for each category. For both neuron types, we produced behavior maps for 100 linearly spaced values of duty cycle (from 1 to 100 %) and for 30 logarithmically distributed values of acoustic pressure amplitudes (from 10 to 600 kPa), using the SONIC model. Note that a typical behavior map was generated in about 30 hours, a process that would have taken more than 10 years with the detailed NICE model.

3.4.1 Regular spiking neuron.

In the sub-threshold state ($Q_m < Q_T$), LIFUS-ON periods of sufficient intensity trigger a strong effective hyperpolarization of several tens of millivolts that closes all voltage-gated ion channels (figure 3(a)), but also triggers a depolarizing leakage current (proportional to the difference $V_{m,eff}$ - E_{leak}) that increases the membrane charge density (figure 7(a), inset i). At each pulse offset, the sudden mechanical stabilization of the membrane prompts an effective depolarization that crosses the leakage reversal potential and brings the membrane potential above its pre-pulse level, yet remaining in the sub-threshold state. Hence, the leakage current changes polarity and the charge density decreases. As a result, the net charge variation over a pulse repetition interval depends on the combination of pressure amplitude and duty cycle (referred to as ultrasonic dose) that determines the magnitude and duration of LIFUS-ON effective depolarization, and is positive for ultrasonic doses above a certain threshold. As the charge density progressively approaches Q_T, effective hyperpolarizations and depolarizations are shifted towards higher potential values, which diminishes the imbalance between the LIFUS-ON and LIFUS-OFF charge variations, ultimately reducing the net charge increase per

pulse repetition interval. Above a critical ultrasonic dose, the imbalance stays positive as the charge crosses Q_T, at which point the sodium channels begin to open and drive further charge increase.
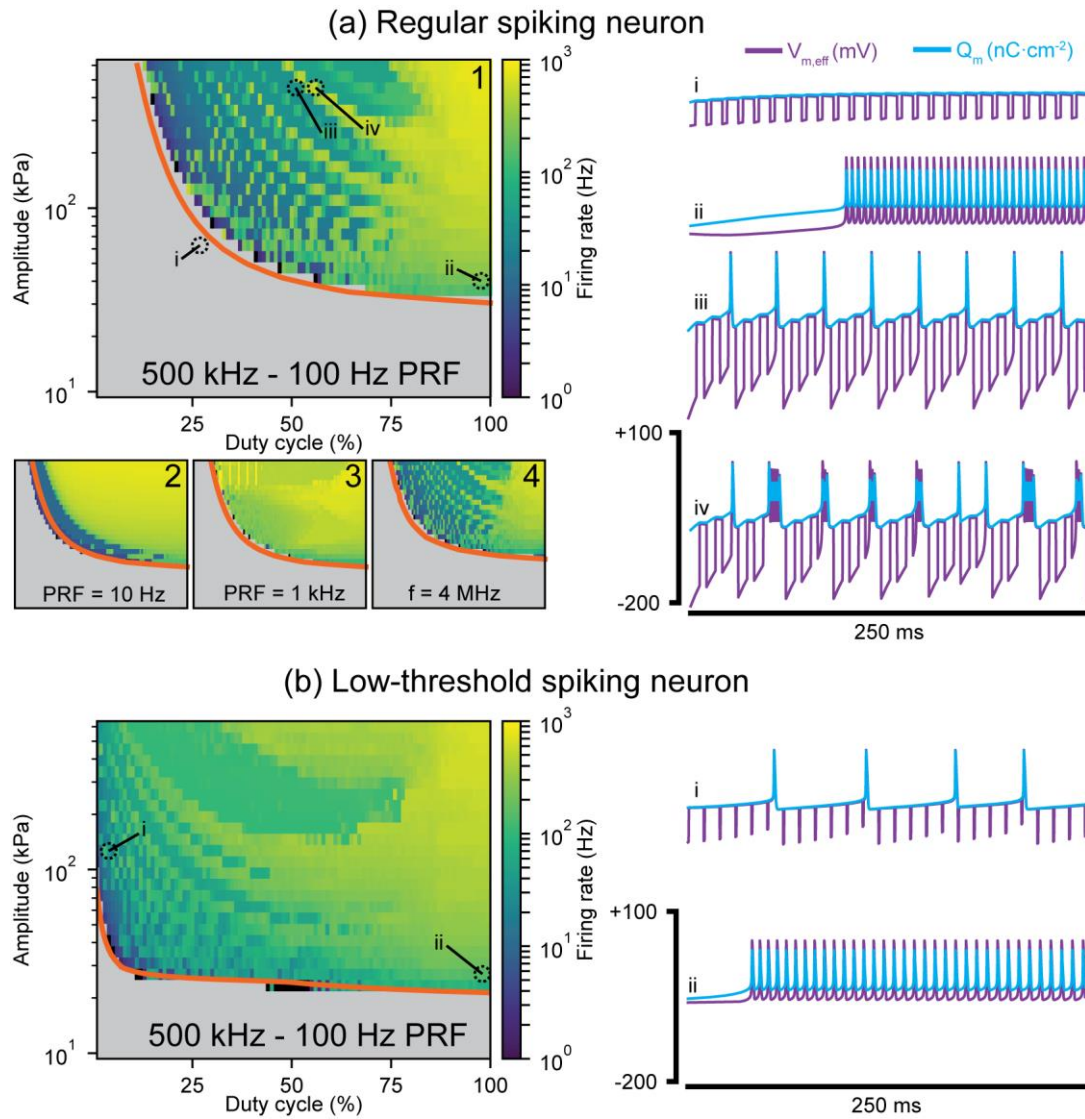

Figure 7. Cell-type-specific LIFUS behavior maps. (a) Left: 2D behavior maps of a RS neuron (32 nm sonophore radius) for various carrier frequency and PRF values, depicting inactivation (gray) and activation (firing rate color code) regions, along with threshold amplitudes at various duty cycles predicted from the quasi-steady state approximation (orange curve). Right: detailed profiles of membrane charge density (black) and effective membrane potential (gray) for selected combinations of duty cycle and amplitude at 500 kHz, 100 Hz PRF. (b) Left: behavior map of a LTS neuron (32nm sonophore radius) at 500 kHz, 100 PRF. Right: detailed profiles for selected duty cycle – amplitude combinations.

As the neuron reaches the supra-threshold state ($Q_m > Q_T$), the effective gating kinetics of sodium and potassium channels during LIFUS-ON periods trigger a high-frequency, non-adaptive train of action potentials (figure 7(a), inset ii) with a high spiking frequency (>> 100 Hz) and reduced spike amplitude (<< 70 nC/cm^2). During LIFUS-OFF periods, the system's behavior mainly depends on its electrical state at the preceding pulse offset: a decreasing membrane charge at the transition tends to induce repolarization, whereas an increasing membrane charge triggers further depolarization towards an action potential of "standard" amplitude through the traditional (i.e., unmodulated) membrane dynamics of the neuron (figure 7(a), inset iii). Thus, the regular spiking neuron depolarizes thanks to a LIFUS-ON leakage current - depending on the effective membrane potential - until a threshold charge value is reached, above

which it fires traditional or modified action potentials depending on the absence or presence of LIFUS stimulus, respectively.

At high ultrasonic doses, the LIFUS-ON system dominance implies that each pulse necessarily triggers several high frequency spikes, thereby producing a bursting behavior synchronized with the PRF manifested by a bimodal firing rate spectrum. At lower doses, several LIFUS pulses are required to bring the charge density above the excitation threshold and trigger an action potential, yielding a firing rate that is lower than the PRF. However, for particular ultrasonic doses, the rate of sub-threshold charge increase is such that the excitation threshold is synchronized with the time of pulse onset, so that several spikes can be fired within the pulse, enriching the firing rate spectrum with a high-frequency component. Interestingly, at intermediate PRF values (100 Hz), such burst elicitation is concomitant with a synchronization of sub-threshold charge increase with a given multiple of the pulse repetition interval (figure 7(a), inset iv) that occurs only for particular combinations of duty cycle and pressure amplitude, seen as distinct stripes of higher firing rate on the behavior map. This singular behavior is not observed at lower and higher PRF values (figure 7(a), maps 2 and 3). In the former case, the increased duration of LIFUS-ON and LIFUS-OFF periods implies that burst elicitation is necessarily phase-locked with the pulse repetition interval itself (as opposed to one of its multiples). In the latter case, pulse repetition intervals are in the order of magnitude of spike duration and therefore do not allow pulse-spike synchronization. Thus, the regular spiking neuron experiences a multimodal firing rate constituted of low and high frequency components under pulsed stimuli, with a singular pulse-burst synchronization at specific ultrasonic doses for intermediate pulse repetition frequencies. This synchronization is however unlikely to occur in nature, as the rate of charge build-up will fluctuate due to noise.

For a given duty cycle, the threshold excitation amplitude is the one required to bring the membrane charge density up to Q_T. At very low DC, such amplitudes are far above 1 MPa and therefore not suitable for LIFUS applications. However, they diminish drastically as the duty cycle is increased to reach acceptable magnitudes of about 100 kPa at 25 % DC, and then stabilize around an asymptotic value as we approach 100 % DC. Interestingly, rheobase amplitudes computed with the quasi-steady state approximation are able to predict this excitation threshold evolution with remarkable accuracy at high enough pulse-repetition frequencies (figure 7(a), orange traces on maps 1 and 3). At 10 Hz PRF, however, the variation of charge density during LIFUS-OFF periods at low duty cycles diverges substantially from the assumed linearity and induces a greater net charge increase per pulse repetition interval, allowing to reach Q_T with smaller pressure amplitudes than predicted at small duty cycles (figure 7(a), map 2). This inacuraccy vanishes as the duty cycle increases above 50 %. As expected, the carrier frequency has very little influence on LIFUS neural responses: only above the MHz range, stronger viscous pressures limiting the extent of sonophore cavitation induce a minor decrease in the magnitude of $V_{m,eff}$, thereby shifting the excitation threshold towards slightly higher ultrasonic

doses (figure 7(a), map 4). Hence, the quasi-steady state approximation provides a reliable estimate of frequency- and duty cycle-dependent threshold excitation amplitudes, for pulse repetition frequencies above 10 Hz.

3.4.2 Low-threshold spiking neuron.

The LTS neuron is intrinsically easier to bring to a supra-threshold state due to its higher resting potential, and is thus generally activated at lower amplitudes than the RS neuron (figure 7(b), map). Moreover, in the sub-threshold state, the sudden effective depolarization at pulse offsets triggers the transient opening of intrinsic low-threshold calcium voltage-gated channels during LIFUS-OFF periods, producing a depolarizing current that can overcome the effect of the hyperpolarizing leakage current and drive further depolarization of the membrane towards Q_T. As a result, the LTS neuron can be excited at far lower duty cycles than the RS neuron with sub-MPa amplitudes (figure 7(b), inset i). Again, the activation threshold curve of the neuron is accurately captured by our quasi-steady state approximation, despite the extensive involvement of the voltage-gated calcium channel in the sub-threshold development of its neural response. (figure 7(b), orange trace on map).

Once in the supra-threshold state, sodium and potassium currents predominate and the neuron behavior is analogous to that of the regular spiking type. Hence, a similar non-adaptive tonic spike train is evoked at high ultrasonic doses (figure 7(b), inset ii). Understandably, regions of burst phase locking with multiples of the pulse repetition interval are shifted towards lower ultrasonic doses, as a result of the neuron's enhanced sub-threshold depolarization ability. Finally, at very low ultrasonic doses permitting frequent repolarization, the effect of a LIFUS pulse is timing-dependent as it can trigger or shut down a sub-threshold calcium-driven depolarization, thereby accelerating or delaying the occurrence of the next spike, and producing a variable low-frequency firing rate. In summary, the low-threshold spiking neuron provides a calcium driven LIFUS-OFF sub-threshold depolarization mechanism that permits excitation at very low duty cycles. Excitation thresholds are accurately predicted by the quasi-steady state approximation despite the increased complexity of sub-threshold dynamics.

4. Discussion

4.1 Interpretability of the SONIC Model

The high degree of similarity between detailed and effective solutions of the NICE and SONIC electromechanical models, respectively, reveals that membrane charge density and ion channels gating variations during a LIFUS neural response can be expressed as a function of "effective" membrane potential and rate constants, averaged over acoustic cycles. These effective variables all exhibit a dependency on Q_m in the absence of acoustic perturbation, and they are amplified upon sonication to an extent that depends directly on acoustic pressure amplitude.

Specifically, the amplification of effective membrane potential induces stronger ionic currents and faster charge variations, while that of gating rate constants triggers faster adaptations of voltage-gated ion channels to a given change in membrane charge density. Together, these two phenomena explain the singular dynamics observed during LIFUS-ON periods (figure 7(a), inset ii): 1) Given that sodium and potassium have reversal potentials of opposite signs (50 and -90 mV, respectively), $V_{m,eff}$ amplification primarily increases the deviation from E_{Na} and thus the magnitude of the depolarizing sodium current when $Q_m < 0$, and deviation from E_K and the magnitude of the hyperpolarizing potassium current when $Q_m > 0$. This sign-dependent, ion specific current amplification limits the charge density variation range, ultimately reducing the amplitude of the depolarization and hyperpolarization peaks reached during action potential trains. 2) The amplification of (i) $\alpha_{m,eff}$ and $\alpha_{n,eff}$ for positive charge densities and (ii) $\beta_{m,eff}$ and $\beta_{n,eff}$ for negative charge densities accelerate the opening and closing of the sodium and potassium activation gates during action potentials, further enhancing their temporal dynamics. 3) $\alpha_{h,eff}$ amplification triggers faster reactivation of the sodium h-gate upon repolarization, which effectively eliminates recovery periods between spikes, thereby considerably increasing the firing frequency to a rate far superior to what can be evoked with electrical stimulation. 4) $\alpha_{p,eff}$ amplification accelerates the p-gate opening upon occurrence of the first spike, yielding a very fast firing rate adaptation within the first few spike intervals, and is therefore responsible for the non-adaptive nature of LIFUS-triggered spike trains.

Beyond the explanation of spike shape modulation, by being able to interpret the charge evolution as a result of effective channel currents, it is possible to identify conditions in which the currents balance out and hence to predict excitation thresholds (see Methods section) without requiring integration of the differential equations.

4.2 Relevance for experimental validation

Despite predicting LIFUS parameter-dependent trends of neural activation and inhibition that match with several experimental results [11,12], one major limitation of the NICE electromechanical model is the lack of direct experimental observation of intramembrane cavitation. Given the nanometer-scale extent of hypothesized bilayer sonophores, recording local oscillations in membrane thickness or transmembrane potential might be elusive, as this would require a sensing technology of high spatial (< 100 nm) and temporal (<< 1 μs) resolution with, in the former case, enough sensitivity to detect thickness variations of a few nanometers. However, the predicted dependency of response latency, neural firing rate and especially spike amplitude on LIFUS parameters are testable features that could provide indirect validation of the NICE electromechanical model. In this context, our SONIC model defines a more interpretable frame of reference (charge density and time-averaged $V_{m,eff}$) supporting the design of such validation experiments and providing additional insight on how exactly LIFUS modulates ion channel gating dynamics.

4.3 Generalizability and integration

The presented coarse-graining approach can be adapted to any neuron model with conductance-based membrane dynamics, provided that response-time constants of its constituent voltage-gated ion channels are in the millisecond range. The translation into effective channel models could be further simplified by neglecting the small-scale changes in deflection profiles across different neuron types, and thus deriving cell-type-specific effective variables from a single pre-computed table of mechanical deflections. Moreover, while we focused here on single neuron characterization, SONIC models of several neuron types could easily be coupled together with synaptic connections in order to design realistic, yet computationally efficient representations of cortical and/or peripheral neural networks responding to LIFUS. These network models could be used to increase our understanding of the influence of different LIFUS parameters on large scale neural response as in [12]. Alternatively, they could guide the design of studies about the causal role of certain brain regions in specific behaviors and behavioral disorders, as LIFUS currently emerges as very compelling technology for causal brain mapping [31].

4.4 Advantage over other simplification strategies

The authors of the NICE electromechanical model have already proposed approaches to tackle the computational inefficiency of the original differential system (equations (1) and (2)), and speed up the numerical integration of solutions. Taking advantage of the system's weak influence of the electrical system on the mechanical one, a hybrid resolution scheme was developed in which the full electromechanical system is periodically (every 500 μs) integrated for a few acoustic cycles until quasi-static (oscillatory) stabilization of the mechanical variables, which are then assumed to remain unchanged for the rest of the 500 μs interval, allowing to integrate a simplified system with reduced stiffness for a large portion of the solution [11]. A later simplification was devised that represents the oscillations of sonophore membrane capacitance by a simple sinusoid at the US frequency, thereby dispensing of the mechanical part of the model [12]. However, as both simplifications explicitly model the high-frequency, large-amplitude oscillations of the transmembrane potential, their integration time step must stay significantly smaller than the acoustic period to ensure convergence, which represents a strongly limiting factor for algorithmic optimization. Conversely, the time step used in our SONIC model is completely independent from the stimulus frequency, and only limited by the order of magnitude of the response time constants of constituent ion channels (as well as the pulse repetition interval). Moreover, despite yielding excitation profiles qualitatively similar to that of the detailed NICE model, the sinusoidal capacity-driven model does not properly capture the asymmetry of capacitance oscillations that dictates the dynamics of the initial charge build-up phase during CW stimulation; therefore, it cannot provide an accurate estimate of the response latency and excitation threshold for such protocols. On the other hand, our SONIC model considers this asymmetry during the pre-computation of lookup tables, and can therefore reliably predict these excitation metrics.

5. Conclusion

In this study, we derived an effective coarse-grained variant of the NICE electromechanical model that greatly accelerates numerical simulations while preserving the accuracy of computed solutions and offering electrophysiological interpretability. This so-called SONIC model was used to explore systematically the LIFUS parametric space and establish cell-type-specific behavior maps, by recasting LIFUS responses under the frame of an "effective" neural dynamics. In ongoing work, we are conducting sonication experiments on isolated leech ganglia and analyzing the electrical responses of specific neurons to LIFUS with intracellular recordings, in order to verify the trends in effective spiking dynamics suggested by the model and provide indirect validation and quantification of the intramembrane cavitation mechanism. We are also integrating this effective coarse-grained approach into the NEURON simulation environment [32], in order to generate spatially extended neuron models with realistic cellular morphology and study the impact of the spatial distribution of LIFUS receptive sub-cellular structures on the neural response.

Acknowledgments

References

[1]   Escoffre J-M and Bouakaz A 2016 *Therapeutic ultrasound*

[2]   Kyriakou A, Neufeld E, Werner B, Paulides M M, Szekely G and Kuster N 2014 A review of numerical and experimental compensation techniques for skull-induced phase aberrations in transcranial focused ultrasound *Int. J. Hyperthermia* **30** 36–46

[3]   Ghanouni P, Pauly K B, Elias W J, Henderson J, Sheehan J, Monteith S and Wintermark M 2015 Transcranial MRI-Guided Focused Ultrasound: A Review of the Technologic and Neurologic Applications *Am. J. Roentgenol.* **205** 150–9

[4]   Deffieux T, Younan Y, Wattiez N, Tanter M, Pouget P and Aubry J-F 2013 Low-intensity focused ultrasound modulates monkey visuomotor behavior *Curr. Biol. CB* **23** 2430–3

[5]   Kim H, Park M Y, Lee S D, Lee W, Chiu A and Yoo S-S 2015 Suppression of EEG visual-evoked potentials in rats through neuromodulatory focused ultrasound *Neuroreport* **26** 211–5

[6]   King R L, Brown J R, Newsome W T and Pauly K B 2013 Effective parameters for ultrasound-induced in vivo neurostimulation *Ultrasound Med. Biol.* **39** 312–31

[7]   Legon W, Sato T F, Opitz A, Mueller J, Barbour A, Williams A and Tyler W J 2014 Transcranial focused ultrasound modulates the activity of primary somatosensory cortex in humans *Nat. Neurosci.* **17** 322–9

[8]   Mueller J, Legon W, Opitz A, Sato T F and Tyler W J 2014 Transcranial focused ultrasound modulates intrinsic and evoked EEG dynamics *Brain Stimulat.* **7** 900–8

[9]   Tyler W J, Tufail Y, Finsterwald M, Tauchmann M L, Olson E J and Majestic C 2008 Remote Excitation of Neuronal Circuits Using Low-Intensity, Low-Frequency Ultrasound *PLOS ONE* **3** e3511

[10]   Younan Y, Deffieux T, Larrat B, Fink M, Tanter M and Aubry J-F 2013 Influence of the pressure field distribution in transcranial ultrasonic neurostimulation *Med. Phys.* **40** 082902

[11]   Plaksin M, Shoham S and Kimmel E 2014 Intramembrane Cavitation as a Predictive Bio-Piezoelectric Mechanism for Ultrasonic Brain Stimulation *Phys. Rev. X* **4**

[12]   Plaksin M, Kimmel E and Shoham S 2016 Cell-Type-Selective Effects of Intramembrane Cavitation as a Unifying Theoretical Framework for Ultrasonic Neuromodulation *eNeuro* **3**

[13]   Kim H, Taghados S J, Fischer K, Maeng L-S, Park S and Yoo S-S 2012 Noninvasive transcranial stimulation of rat abducens nerve by focused ultrasound *Ultrasound Med. Biol.* **38** 1568–75

[14]   Kim H, Chiu A, Lee S D, Fischer K and Yoo S-S 2014 Focused Ultrasound-mediated Non-invasive Brain Stimulation: Examination of Sonication Parameters *Brain Stimulat.* **7** 748–56

[15]   Tufail Y, Yoshihiro A, Pati S, Li M M and Tyler W J 2011 Ultrasonic neuromodulation by brain stimulation with transcranial ultrasound *Nat. Protoc.* **6** 1453–70

[16]   Yoo S-S, Bystritsky A, Lee J-H, Zhang Y, Fischer K, Min B-K, McDannold N J, Pascual-Leone A and Jolesz F A 2011 Focused ultrasound modulates region-specific brain activity *NeuroImage* **56** 1267–75

[17]   Krasovitski B, Frenkel V, Shoham S and Kimmel E 2011 Intramembrane cavitation as a unifying mechanism for ultrasound-induced bioeffects *Proc. Natl. Acad. Sci. U. S. A.* **108** 3258–63

[18]   Plesset M S 1949 The Dynamics of Cavitation Bubbles *J. Appl. Mech.* **16** 277–82

[19]   Pospischil M, Toledo-Rodriguez M, Monier C, Piwkowska Z, Bal T, Frégnac Y, Markram H and Destexhe A 2008 Minimal Hodgkin-Huxley type models for different classes of cortical and thalamic neurons *Biol. Cybern.* **99** 427–41

[20]   Wong H Y 1977 *Handbook of essential formulae and data on heat transfer for engineers* (London ; New York: Longman)

[21]   Boal D 2012 *Mechanics of the Cell* (Cambridge, UK ; New York: Cambridge University Press)

[22]   IT'IS Foundation 2015 Tissue Properties Database V3.0

[23]   Phillips R, Ursell T, Wiggins P and Sens P 2009 Emerging roles for lipids in shaping membrane-protein function *Nature* **459** 379–85

[24]   Rawicz W, Olbrich K C, McIntosh T, Needham D and Evans E 2000 Effect of chain length and unsaturation on elasticity of lipid bilayers. *Biophys. J.* **79** 328–39

[25]   Sun R, Hu W and Duan Z 2001 Prediction of Nitrogen Solubility in Pure Water and Aqueous NaCl Solutions up to High Temperature, Pressure, and Ionic Strength *J. Solut. Chem.* **30** 561–73

[26]   GENG M and DUAN Z 2010 Prediction of oxygen solubility in pure water and brines up to high temperatures and pressures *Geochim. Cosmochim. Acta* **74** 5631–40

[27]   Wise D L and Houghton G 1966 The diffusion coefficients of ten slightly soluble gases in water at 10–60°C *Chem. Eng. Sci.* **21** 999–1010

[28]   Mohr P J, Taylor B N and Newell D B 2008 CODATA recommended values of the fundamental physical constants: 2006 *Rev. Mod. Phys.* **80** 633–730

[29]   Destexhe A, Contreras D, Steriade M, Sejnowski T J and Huguenard J R 1996 In vivo, in vitro, and computational analysis of dendritic calcium currents in thalamic reticular neurons *J. Neurosci. Off. J. Soc. Neurosci.* **16** 169–85

[30]   Destexhe A, Neubig M, Ulrich D and Huguenard J 1998 Dendritic low-threshold calcium currents in thalamic relay cells *J. Neurosci. Off. J. Soc. Neurosci.* **18** 3574–88

[31]   Kubanek J 2018 Neuromodulation with transcranial focused ultrasound *Neurosurg. Focus* **44** E14

[32]   Hines M L and Carnevale N T 1997 The NEURON simulation environment *Neural Comput.* **9** 1179–209